Massive Dirac fermion behavior in a low bandgap graphene nanoribbon near a topological phase boundary

*Qiang Sun[1], Oliver Gröning[1], Jan Overbeck[1,3], Oliver Braun[1,3], Mickael L. Perrin[1], Gabriela Borin Barin[1], Maria El Abbassi[1], Kristjan Eimre[1], Edward Ditler[1], Colin Daniels[4], Vincent Meunier[4], Carlo A. Pignedoli[1], Michel Calame[1,3], Roman Fasel[1,2], Pascal Ruffieux[1]**

Dr. Q. Sun, Dr. O. Gröning, J. Overbeck, O. Braun, Dr. M. L. Perrin, Dr. G. B. Barin, Dr. M. El Abbassi, K. Eimre, E. Ditler, Dr. C. A. Pignedoli, Prof. M. Calame, Prof. R. Fasel, Dr. P. Ruffieux
Empa, Swiss Federal Laboratories for Materials Science and Technology
8600 Dübendorf, Switzerland
E-mail: pascal.ruffieux@empa.ch

Prof. R. Fasel
Department of Chemistry and Biochemistry
University of Bern
3012 Bern, Switzerland

J. Overbeck, O. Braun, Prof. M. Calame
Department of Physics
University of Basel
Klingelbergstrasse 80, 4056 Basel, Switzerland

C. Daniels, Prof. V. Meunier
Rensselaer Polytechnic Institute,
Department of Physics, Applied Physics and Astronomy
Troy, New York 12180, United States

Keywords: graphene nanoribbon, topological materials, scanning tunneling microscopy and spectroscopy, electronic structure

Abstract: Graphene nanoribbons (GNRs) have attracted much interest due to their largely modifiable electronic properties. Manifestation of these properties requires atomically precise GNRs which can be achieved through a bottom-up synthesis approach. This has recently been applied to the synthesis of width-modulated GNRs hosting topological electronic quantum phases, with valence electronic properties that are well captured by the Su-Schrieffer-Heeger (SSH) model describing a one-dimensional chain of interacting dimers. Here, an ultra-low bandgap GNRs with charge carriers behaving as massive Dirac fermions can be realized when their valence electrons represent an SSH chain close to the topological phase boundary, i.e. when the intra- and inter-dimer coupling become approximately equal. Such a system has been

achieved via on-surface synthesis based on readily available pyrene-based precursors and the resulting GNRs are characterized by scanning probe methods. The pyrene-based GNRs (pGNRs) can be processed under ambient conditions and incorporated as the active material in a field effect transistor. A quasi-metallic transport behavior is observed at room temperature, whereas at low-temperature the pGNRs behave as quantum dots showing single-electron tunneling and Coulomb blockade. This study may enable the realization of devices based on carbon nanomaterials with exotic quantum properties.

The last decade has brought significant advances in the bottom-up fabrication of atomically precise graphene nanomaterials[1] and structures of increasing complexity.[2–4] While GNRs with zigzag edges (ZGNRs) so far have not been integrated into devices due to their reactivity, major progress in the processing of GNRs with armchair edges (AGNRs) has been achieved, and field effect transistors (FETs) that exploit their sizable electronic bandgaps have recently been reported.[5,6] However, the large bandgaps of the currently available AGNRs severely limit device performances due to significant Schottky barriers at the contacts. The synthesis of GNRs with smaller bandgaps would hence be highly desirable. To this end, width-modulated AGNRs are promising candidates, because their periodically arranged and overlapping electronic states give rise to one-dimensional topological bands within the bandgap of the pristine AGNR backbone.[7,8] According to the SSH model, their fundamental electronic properties such as bandgap, band width, and topological class can be widely tuned by varying the intra- and the inter-dimer coupling strength which are related to the overlap between the corresponding electronic states located at the ribbon edge extension. Exploiting this concept, we show that for a GNR obtained by a specific intermolecular fusion of pyrene subunits (pGNR), the intra-dimer coupling describing the frontier electronic states of the pyrene subunit and the inter-dimer coupling describing the coupling between them are almost identical. This results in an ultra-

low bandgap of ~ 0.2 eV as confirmed by scanning tunneling spectroscopy (STS). Finally, we demonstrate the integration of pGNRs as active channel material in FET devices.

On-surface synthesis of pGNRs is achieved by activation of 1,6-dibromopyrene[9] on Au(111) under ultrahigh vacuum conditions. The reaction route, illustrated in **Figure 1a**, follows two surface-assisted steps including dehalogenative homocoupling to yield an intermediate polymer and cyclodehydrogenation to form the fully conjugated ribbon. Polymerization is achieved by annealing the sample to 180 ºC (Figure 1b and Supplementary Section 1). As shown in the close-up STM image and the superimposed chemical models in Figure 1b, the alternating up-down tilting of the pyrene units matches well with the alternating STM protrusions along the polymers. The second annealing step (300 ºC) induces cyclodehydrogenation of the intermediate polymer via the rotation of every second pyrene unit within the polymer chain and results in planar pGNRs (Figure 1c). For a more detailed discussion of the reaction pathway, we refer to the Supplementary Section 2. The formation of the targeted pGNR can be unambiguously verified by high-resolution STM imaging and bond-resolved nc-AFM imaging (Figure 1d).[10,11]

To determine the electronic properties of the pGNR, we first compute its band structure by DFT calculations. Its bandgap is found to be as small as 0.18 eV (Figure 1e), significantly less than the DFT calculated bandgap of ~0.4 eV for the "quasi-metallic" 5-AGNR.[12] Experimentally, the electronic properties of the pGNR can be probed by STS. We have performed differential conductance dI/dV spectroscopy of a pGNR with a length of ~17 nm (**Figure 2a** and 2b), which provides information on the local density of states (LDOS). The red spectrum taken in the middle of the pGNR (marked by a red cross in Figure 2b) exhibits three pronounced peaks at low bias voltages, whereas spectra taken at the termini of the ribbon (marked by a blue cross in Figure 2b) show barely any resonance peaks. The spatial distribution of the frontier electronic states revealed in Fig. 2a is obtained from a series of point spectra taken along the ribbon as indicated by the green line in Figure 2b. We note that the assignment

of the peaks observed around the Fermi level in Figure 2a to their corresponding bands is not straightforward, as the difference in workfunctions of GNRs and metal surfaces usually causes a shift in energy of the electronic states of surface-bound GNRs.[13,14] Nevertheless, the observed electronic states can be identified from their characteristic spatial distribution, as finite-length effects, i.e. the scattering of electrons at the ribbon ends, allow imaging of the resulting standing wave patterns via dI/dV mapping (Figure 2c).[15,16] Here, the contrast of the differential conductance map is enhanced by functionalizing the tip with a CO molecule. As shown in Figure 2c, two distinct standing wave patterns are observed at bias voltages of 70 mV and -30 mV, which correspond to the first and second confined states, i.e. the HOMO (onset of VB) and HOMO-1 of the finite ribbon. This assignment is corroborated by comparing the dI/dV maps with the DFT calculated LDOS maps of the corresponding molecular orbitals (Figure 2c). Note that the nodal patterns in the STS maps are different from those by DFT because the CO-functionalized tip was not taken into account in the simulations. The next higher energy state at 300 mV is thus identified to be the LUMO (onset of CB), which translates into a bandgap of 230 mV.

With the frontier states of the pGNR being identified, we proceed with the acquisition and analysis of data for pGNRs of different lengths, which allows for a determination of the pGNR electronic gap as a function of ribbon length (Figure S3). We find that the electronic gap of the pGNR on Au(111) converges to 230 mV with increasing ribbon length (the longest ribbon we measured consists of 37 pyrene units, i.e. a length of ~24.5 nm). The decrease of the electronic gap with ribbon length is qualitatively well reproduced by DFT calculations (Figure S4 a,b), although they predict a somewhat slower decrease. Importantly, the measured gap of the pGNR on Au(111) of 230 mV represents the smallest bulk bandgap of all GNRs that have so far been synthesized and studied on surfaces.

To rationalize the origin of the small bandgap and the linearly dispersing bands of the pGNR, we devise a description of the frontier bands in the framework of a 2-band SSH model (**Figure**

3). At the basis of this description is the assumption that the HOMO and LUMO of the pyrene subunit can be viewed as bonding and anti-bonding dimer states of the SSH chain. Figure 3b illustrates the corresponding decomposition of the bonding HOMO state $|\Psi_{bond}\rangle$ and the antibonding LUMO state $|\Psi_{anti}\rangle$ to obtain the A and B sub-lattice polarized zero-energy mode wave functions $|\hat{A}_i\rangle = \frac{1}{\sqrt{2}}[|\Psi_{bond}\rangle + |\Psi_{anti}\rangle]$ and $|\hat{B}_i\rangle = \frac{1}{\sqrt{2}}[|\Psi_{bond}\rangle - |\Psi_{anti}\rangle]$. The latter will form the basis states of the SSH chain. At nearest neighbor TB level of theory $|\hat{A}_i\rangle$ and $|\hat{B}_i\rangle$ are fully determined by three wave function amplitudes $\gamma = 0.521$, $\delta = 0.418$ and $\varepsilon = 0.232$ (Figure 3c and 3d). Accordingly, we can write the elements of the SSH Hamiltonian in terms of the carbon $2p_z$ nearest-neighbor hopping parameter $\gamma_0 \approx 3\ eV$ as follows:

$$\langle \hat{A}_i | H | \hat{A}_i \rangle = \langle \hat{B}_i | H | \hat{B}_i \rangle = \langle \hat{A}_i | H | \hat{A}_{i+1} \rangle = \langle \hat{B}_i | H | \hat{B}_{i+1} \rangle = 0 \quad (1)$$

$$\langle \hat{A}_i | H | \hat{B}_i \rangle = \langle \hat{B}_i | H | \hat{A}_i \rangle = (2\varepsilon(\gamma - \delta) + \delta^2) \cdot 2\gamma_0 = \frac{E_{g,py}}{2} = 0.445\gamma_0 = t_n \quad (2)$$

$$\langle \hat{A}_i | H | \hat{B}_{i+1} \rangle = \langle \hat{B}_i | H | \hat{A}_{i+1} \rangle = (\gamma^2 + \delta^2) \cdot \gamma_0 = 0.446\gamma_0 = t_m \quad (3)$$

Equation 1 is a direct consequence of the sub-lattice polarization of the zero-energy mode wave functions. With $c_{A_i}^\dagger$, $c_{B_i}^\dagger$, c_{A_i}, c_{B_i} denoting the creation and annihilation operators of the zero-energy modes at pyrene site i, we find:

$$H = -\sum_i t_n \left[c_{A_i}^\dagger c_{B_i} + c_{B_i}^\dagger c_{A_i}\right] - \sum_{<i,j>} t_m \left[c_{A_i}^\dagger c_{B_j} + c_{B_i}^\dagger c_{A_j}\right] \quad (4)$$

where $< i, j >$ denotes the sum over neighboring sites. This is exactly the SSH Hamiltonian leading to the dispersion relation

$$E(k) = \pm\sqrt{t_n^2 + t_m^2 \pm 2t_n t_m \cos(ak)} \quad (5)$$

considering that we have 2 pyrene molecules in the unit cell and therefore 4 bands (see also Supplementary Section 4). The fact that the inter-pyrene coupling strength t_m = $1.002 t_n$ is

almost identical to the intra-pyrene coupling constant t_n has important implications for the electronic properties of the pGNR. In **Figure 4a** the DOS is plotted as a function of t_m according to the SSH dispersion relation (Equation 5). For $t_m = 0$, the situation of isolated pyrene units with a HOMO-LUMO gap of $E_{g,py} = 2t_n$ is reproduced. For increasing t_m, the bandgap decreases and fully closes when $t_m = t_n$. This metallic case also marks the topological phase boundary separating the topologically trivial phase with $t_m < t_n$ from the topologically non-trivial phase with $t_m > t_n$. This implies that systems with almost equal coupling constants t_m and t_n are naturally located close to the topological phase boundary and have a small bandgap given by $E_g = 2|t_m - t_n|$. TB calculations of the full structure (i.e. with 32 $2p_z$-orbitals per unit cell) predict the pGNR to have a small gap and to be topologically trivial (Figure S8) with $t_m \approx 0.86t_n$, i.e. slightly smaller than the minimal 2-orbital SSH model. Figure 4b shows the different wave functions of the HOMO between topologically trivial and non-trivial pGNR by TB calculations. The absence of end states at the termini of the pGNRs in experiment confirms their topologically trivial nature.[7,17]

In the limit of almost equal coupling constants t_n and t_m, the band dispersion of SSH bands, given by Equation 5 can be simplified to

$$E(k) = \pm\sqrt{\delta t^2 + (tak)^2} \qquad (6)$$

with $t = t_n$ and $\delta t = t_m - t_n$. Comparison of this simplified dispersion relation with the SSH bands confirms excellent agreement for small differences between intra- and inter-pyrene coupling constants ($\delta t/t = 0.1$, Figure 4c). Interestingly, this approximation corresponds to the dispersion relation of massive Dirac fermions with

$$E(k) = \pm\sqrt{(mv_F^2)^2 + (\hbar k v_F)^2} \qquad (7)$$

where m is the effective Dirac mass and v_F is the charge carrier velocity. Accordingly, all relevant electronic properties are fully determined by δt and t, yielding $v_F = ta/\hbar$, $m = \delta t/v_F^2$ and a bandgap of $E_g = 2\delta t$. Furthermore, the topological class depends on the sign of

δt, i.e. on whether the intra- SSH-dimer coupling is larger or smaller than the inter- SSH-dimer coupling.

In order to access experimentally the band dispersion of the VB and the CB of the pGNR, we determine the energy positions of the occupied and unoccupied states for pGNRs of different lengths by taking dI/dV spectra, and plot them versus $k = \pm\, p\,\pi/\big((N+1)a\big)$, where the wave vector is associated with the 1D-confined frontier states (see discussions in Figure S4). Here, N is the number of pyrene units constituting the finite-length pGNR, p is the order of the confined frontier states, a is the length of the repeat unit equal to 0.65 nm and (N+1)a approximates the effective pGNR length. The resulting band dispersions of VB and CB (Figure 4d) are in good agreement with the DFT calculation for infinite-length pGNR (Figure 1e). By fitting the experimental VB and CB dispersion data (Figure 4d) with Equation 7 describing the massive Dirac fermions, a bandgap of E_g = 0.12 eV and an effective mass of m = 0.02 m_e are obtained, where m_e is the electron rest mass. The small effective mass is in good agreement with the one extracted from the fit of a massive Dirac fermion to the DFT result (Figure S5).

The small but finite bandgap of the pGNR calls for exploring its performance in an FET configuration. The first step towards device integration is to demonstrate the robustness of pGNRs under ambient conditions. We use Raman spectroscopy to verify the structural integrity of the ribbons after exposing them to air. **Figure 5a** shows the Raman spectrum of pGNRs obtained directly on the Au/mica substrate. We compare this to DFT Raman calculations which allow us to attribute the Raman peaks to specific phonon modes of pGNR (Figure 5a and Figure S10). We find a low energy acoustic mode at 450 rel. cm^{-1} which we labelled RBLM* in analogy to the radial breathing-like mode of AGNRs. We also observe well-defined edge-related modes in the spectral region labelled CH. These modes are characteristic fingerprints of the particular width and edge structure of this ribbon, and their presence after exposure to air strongly suggests the ribbons are stable under ambient conditions.[18–20] The observed

wavelength dependence (Figure S11) points towards an optical resonance in the infrared, in accordance with the low bandgap of the pGNR.

Electronic device fabrication requires the transfer of GNRs to suitable substrates with pre-patterned electrodes.[19,20] We monitor this transfer process by Raman spectroscopy to verify the ribbon integrity. Comparison of the spectra in Figure 5a shows the similarity of the spectral profiles before and after substrate transfer. While the observed change for the lowest frequency CH-mode indicates some modifications of the transferred GNR-film possibly caused by either edge modifications at the (more reactive) pGNR edge or an upshift of the same mode through interactions with the environment,[21] the continued presence of the characteristic RBLM* indicates that the overall structure of the pGNRs remains largely unaffected by the processing (Figure S10). Atomic force microscopy imaging of transferred pGNR-films on Al_2O_3 under ambient conditions reveals a high coverage of GNR bundles and a uniform pGNR-film across the transferred area (Figure 5b). Similar AFM topography was observed for transferred 9-armchair-edge GNRs on Al_2O_3.[20]

Finally, pGNRs are integrated into FET devices in order to probe their electrical properties by measuring the current as a function of both the bias and gate voltage. Graphene is used as electrode material because of its atomic flatness. This allows a 'GNRs-last' fabrication process that avoids additional processing steps with the potential to introduce defects in the transferred pGNRs films (see Methods). Nanogaps are formed by electrical breakdown of a 400 nm wide prepatterned graphene channel, resulting in electrode separations of only a few nanometers.[22,23] As the nanogap size is smaller than the average length of straight ribbon segments (Figure 1c), this allows us to probe transport properties we deem to be representative of the intrinsic ribbon properties.

At room temperature, we observe a linear dependence of the current on the applied bias voltage, and a negligible dependence of the applied gate (Figure S12). We attribute this quasi-metallic behavior to the small bandgap of the pGNR. Figure 5c/d displays transport

measurements at low temperature (9 K). In the I-V curves we observe Coulomb blockade of charge transport at low bias voltages. The onset of current at higher bias is tunable via the applied gate voltage. This is attributed to transport channels of the pGNRs entering the bias window. We observe currents of up to 10 nA at 0.7 V bias (Figure S12c) which we assume to be limited by coupling of the graphene electrodes to the pGNR channel. Figure 5d shows the corresponding stability diagram (differential conductance dI/dV as a function of bias and gate voltages) in which diamond-like features are visible.[24,25] These Coulomb diamonds are characteristic of weakly coupled quantum dots, while the presence of multiple overlapping diamonds suggests that transport occurs through several pGNRs.[26] The observed blockade regions range from ~0.2 to ~0.75 V bias (see Supplementary Section 6 for additional devices). This agrees well with the range of transport gaps expected for pGNRs if one takes into account GW-corrections for electron-electron interaction, the insulating substrate and the range of observed ribbon lengths (Figure S3).

In conclusion, inspired by the principle of topological band engineering,[7,8] we have demonstrated a new kind of GNR with an extremely low bandgap which is even lower than the one of the "quasi-metallic" 5-AGNR that has a similar width. This GNR has mixed armchair and zigzag edge structure, and the origin of its low bandgap can be rationalized within a SSH-type model. Through on-surface synthesis and using a commercially available molecular precursor, we have successfully synthesized the targeted GNR on Au(111) and verified its predicted electronic properties. The experimentally determined band structure of the GNR can be well described by the dispersion relation for massive Dirac fermions, which gives an effective mass of 0.02 m_0 and a bandgap of 0.12 eV. Such ultralow bandgap has independently been confirmed by low-temperature transport measurements in the single-electron tunneling regime with the ribbons integrated into graphene-electrode FETs. These results are of both fundamental interest in designing GNRs with desired electronic properties and/or exhibiting

specific quantum states, and of technological interest in view of the ultimate realization of high-performance GNR devices.

Experimental Section

STM/STS and nc-AFM characterization: A commercial low-temperature STM/AFM (Scienta Omicron) system was used for sample preparation and *in situ* characterization under ultra-high vacuum conditions (base pressure below 1×10^{-10} mbar). Au(111) single crystal and 200 nm Au(111) on Mica substrates were cleaned by standard argon sputtering and annealing cycles. The molecular precursor 1,6-dibromopyrene was purchased from TCI Chemicals. Deposition of the molecular precursors was carried out by thermal evaporation from a 6-fold organic evaporator (Mantis GmbH). STM images were recorded in constant-current mode, and the dI/dV spectra were recorded using the lock-in technique (U_{RMS} = 20 mV). nc-AFM images were recorded with a CO-functionalized tip attached to a quartz tuning fork sensor (resonance frequency 23.5 kHz, oscillation amplitude ~ 80 pm).

Tight-binding calculations: The calculations of the molecular π-electron system have been performed by numerically solving the usual nearest neighbor hopping Hamiltonian considering only the C $2p_z$ orbitals:

$$\widehat{H} = -\gamma_0 \sum_{\langle\alpha,\beta\rangle} c_\alpha^\dagger \, c_\beta^-$$

With $c_\alpha^\dagger$ and c_α^- denoting the usual creation and annihilation operators on site α and $\langle\alpha,\beta\rangle$ denoting the sum over neighboring atomic sites.

DFT calculations on the LDOS maps and bandgaps of pGNRs: The band structure of pGNR were calculated with the Quantum Espresso software package.[27] We used the PBE parameterization for the exchange correlation functional.[28] A cutoff of 400 Ry was used for the plane waves expansion of the charge density. For the representation of the ionic potentials

we used PAW pseudopotentials derived from the SSSP library.[29] Calculations were done within the AiiDA platform.[30]

The CP2K code[31] was used to produce the orbital mappings and the band gaps of the finite-length pGNRs. The electronic states were expanded with a TZV2P Gaussian basis set.[32] We used the PBE exchange correlation functional[28]. A cutoff of 600 Ry was used for the plane wave basis set and norm conserving Goedecker-Teter-Hutter pseudopotentials[33] were used to represent the frozen core electrons of the atoms. The simulation cell was determined by adding 18 Å in each dimension to the molecular bounding box to decouple the periodic images. The geometries of the gas-phase systems were optimized until forces were lower than 0.005 eV/Å.

GNR transfer and ambient AFM imaging: pGNRs were grown on 200 nm Au(111)/mica (Phasis, Switzerland) and transferred to different target substrates using the polymer-free method.[21] We used Al_2O_3 (Crystal GmbH) as target substrate for atomic force microscopy (AFM) measurements. AFM (Bioscope, Bruker) was performed in ambient conditions using tapping mode and silicon probes (OPUS model 160AC-SG Ultrasharp Cantilever) with tip radius < 1 nm (force constant ~26 N m^{-1}, resonance frequency in the range of 300 kHz). Phase diagrams were recorded with scan size of 1.5 μm and scan speed of 1 Hz. AFM images under ambient condition were analyzed using WSxM software.[34]

Raman Spectroscopy and DFT calculations: Raman spectra were acquired with a WITec confocal Raman microscope (WITec Alpha 300R) equipped with a home-built vacuum chamber at pressures below 10^{-2} mbar. Imaging conditions were optimized independently for each laser wavelength and substrate to yield optimum signal-to-noise while avoiding laser-induced changes to the GNRs (see Supplementary Table T1 / Figure S10).[35] Signatures of cosmic rays and a polynomial background were subtracted from the spectra.

Theoretical normal modes and associated Raman intensities were calculated using the Phonopy program package[36] in conjunction with DFT and in-house utility codes. For all DFT calculations the program VASP[37–39] was used with projector-augmented-wave pseudopotentials,[40] a plane-wave cutoff of 600 eV, and the Perdew–Burke–Ernzerhof exchange-correlation functional.[28] Initially, the structure was relaxed in DFT until residual forces were less than 10^{-4} eV/Å in magnitude. Phonopy was then used to calculate the phonon mode eigenvectors and frequencies by way of the finite displacement method,[36] where the required force calculations were again obtained from DFT. For each normal mode, associated resonant Raman intensities were modeled utilizing the normal mode displacements along with a finite difference scheme[41] to calculate the derivatives of the frequency dependent dielectric matrix obtained from DFT.[42]

Fabrication and electrical characterization of the FET: Standard Si/SiO_2 (highly p-doped, 0.001 Ohm*cm) with a thermally grown SiO_2 (285 nm) was used as the substrate. Metal pads were defined using electron-beam lithography in PMMA 50K/950K followed by a metallization step (5 nm Ti/40 nm Pt).[5] Chemical vapor deposition (CVD)-grown graphene (Graphenea) was transferred on top and patterned into 400 nm wide stripes using reactive ion etching (Ar/O_2) after another step of e-beam lithography. Sub-5 nm-gaps were formed in the graphene stripes using the electrical breakdown technique.[22,23] Before transferring the ribbons, the graphene gaps were electrically characterized to ensure successful gap formation (see Figure S13). Last, pGNRs were transferred as described above.

The fabricated FETs were characterized in a probe station (Lake Shore Cryotronics, Model CRX-6.5K) under vacuum ($<10^{-6}$ mbar). We employed a data acquisition board (National Instruments USB-6289) to apply the bias and gate voltages and read the voltage output of a custom-made I-V converter (Model SP983, Electronics Lab at the Department of Physics, University of Basel).

Supporting Information
Supporting Information is available from the Wiley Online Library or from the author.

Acknowledgements
This work was supported by the Swiss National Science Foundation under Grant No. 200020_182015, the NCCR MARVEL funded by the Swiss National Science Foundation (51NF40-182892), the Euro-pean Union's Horizon 2020 research and innovation programme under grant agreement number 785219 (Graphene Flagship Core 2), the Office of Naval Research (N00014-18-1-2708), and by a grant from the Swiss National Supercomputing Centre (CSCS) under project ID s746 and s904. Q.S. acknowledges the EMPAPOSTDOCS-II programme under the Marie Sklodowska-Curie grant agreement No 754364, and Yinyin Lin for her support. J.O. and M.C. acknowledge funding by the Swiss Nanoscience Institute.
O.B. acknowledges technical support from the Binning and Rohrer Nanotechnology Center (BRNC), in particular Antonis Olziersky for e-beam lithography. J.O. acknowledges technical support by Sascha Martin and Heinz Breitenstein in designing the vaccum chamber for Raman spectroscopy. C.D. and V.M. acknowledge support from the Office of Naval Research. DFT Raman calculations were performed in part using supercomputing resources provided by the Center for Computational Innovations (CCI) at Rensselaer Polytechnic Institute.

Received: ((will be filled in by the editorial staff))
Revised: ((will be filled in by the editorial staff))
Published online: ((will be filled in by the editorial staff))

References

[1] J. Cai, P. Ruffieux, R. Jaafar, M. Bieri, T. Braun, S. Blankenburg, M. Muoth, A. P. Seitsonen, M. Saleh, X. Feng, K. Müllen, R. Fasel, *Nature* **2010**, *466*, 470.

[2] S. Kawai, S. Saito, S. Osumi, S. Yamaguchi, A. S. Foster, P. Spijker, E. Meyer, *Nat. Commun.* **2015**, *6*, 8098.

[3] Z. Pedramrazi, C. Chen, F. Zhao, T. Cao, G. D. Nguyen, A. A. Omrani, H.-Z. Tsai, R. R. Cloke, T. Marangoni, D. J. Rizzo, T. Joshi, C. Bronner, W.-W. Choi, F. R. Fischer, S. G. Louie, M. F. Crommie, *Nano Lett.* **2018**, *18*, 3550.

[4] J. Liu, B.-W. Li, Y.-Z. Tan, A. Giannakopoulos, C. Sanchez-Sanchez, D. Beljonne, P. Ruffieux, R. Fasel, X. Feng, K. Müllen, *J. Am. Chem. Soc.* **2015**, *137*, 6097.

[5] J. P. Llinas, A. Fairbrother, G. B. Barin, W. Shi, K. Lee, S. Wu, B. Y. Choi, R. Braganza, J. Lear, N. Kau, W. Choi, C. Chen, Z. Pedramrazi, T. Dumslaff, A. Narita, X. Feng, K. Müllen, F. Fischer, A. Zettl, P. Ruffieux, E. Yablonovitch, M. Crommie, R. Fasel, J. Bokor, *ArXiv160506730 Cond-Mat* **2016**.

[6] P. B. Bennett, Z. Pedramrazi, A. Madani, Y.-C. Chen, D. G. de Oteyza, C. Chen, F. R. Fischer, M. F. Crommie, J. Bokor, *Appl. Phys. Lett.* **2013**, *103*, 253114.

[7] O. Gröning, S. Wang, X. Yao, C. A. Pignedoli, G. Borin Barin, C. Daniels, A. Cupo, V. Meunier, X. Feng, A. Narita, K. Mullen, P. Ruffieux, R. Fasel, *Nature* **2018**, *560*, 209.

[8] D. J. Rizzo, G. Veber, T. Cao, C. Bronner, T. Chen, F. Zhao, H. Rodriguez, S. G. Louie, M. F. Crommie, F. R. Fischer, *Nature* **2018**, *560*, 204.

[9] M. Smerieri, I. Píš, L. Ferrighi, S. Nappini, A. Lusuan, C. Di Valentin, L. Vaghi, A. Papagni, M. Cattelan, S. Agnoli, E. Magnano, F. Bondino, L. Savio, *Nanoscale* **2016**, *8*, 17843.

[10] F. J. Giessibl, *Rev. Sci. Instrum.* **2019**, *90*, 011101.

[11] L. Gross, F. Mohn, N. Moll, P. Liljeroth, G. Meyer, *Science* **2009**, *325*, 1110.

[12] L. Yang, C.-H. Park, Y.-W. Son, M. L. Cohen, S. G. Louie, *Phys. Rev. Lett.* **2007**, *99*, 186801.

[13] N. Merino-Díez, A. Garcia-Lekue, E. Carbonell-Sanromà, J. Li, M. Corso, L. Colazzo, F. Sedona, D. Sánchez-Portal, J. I. Pascual, D. G. de Oteyza, *ACS Nano* **2017**, *11*, 11661.

[14] P. Ruffieux, J. Cai, N. C. Plumb, L. Patthey, D. Prezzi, A. Ferretti, E. Molinari, X. Feng, K. Müllen, C. A. Pignedoli, R. Fasel, *ACS Nano* **2012**, *6*, 6930.

[15] E. Carbonell-Sanromà, P. Brandimarte, R. Balog, M. Corso, S. Kawai, A. Garcia-Lekue, S. Saito, S. Yamaguchi, E. Meyer, D. Sánchez-Portal, J. I. Pascual, *Nano Lett.* **2017**, *17*, 50.

[16] H. Söde, L. Talirz, O. Gröning, C. A. Pignedoli, R. Berger, X. Feng, K. Müllen, R. Fasel, P. Ruffieux, *Phys. Rev. B* **2015**, *91*, 045429.

[17] T. Cao, F. Zhao, S. G. Louie, *Phys. Rev. Lett.* **2017**, *119*, 076401.

[18] I. A. Verzhbitskiy, M. D. Corato, A. Ruini, E. Molinari, A. Narita, Y. Hu, M. G. Schwab, M. Bruna, D. Yoon, S. Milana, X. Feng, K. Müllen, A. C. Ferrari, C. Casiraghi, D. Prezzi, *Nano Lett.* **2016**, *16*, 3442.

[19] J. Overbeck, G. B. Barin, C. Daniels, M. Perrin, L. Liang, O. Braun, R. Darawish, B. Burkhardt, T. Dumslaff, X.-Y. Wang, others, *Phys. Status Solidi B* **2019**.

[20] G. Borin Barin, A. Fairbrother, L. Rotach, M. Bayle, M. Paillet, L. Liang, V. Meunier, R. Hauert, T. Dumslaff, A. Narita, others, *ACS Appl. Nano Mater.* **2019**, *2*, 2184.

[21] A. Fairbrother, J.-R. Sanchez-Valencia, B. Lauber, I. Shorubalko, P. Ruffieux, T. Hintermann, R. Fasel, *Nanoscale* **2017**, *9*, 2785.

[22] M. El Abbassi, L. Pósa, P. Makk, C. Nef, K. Thodkar, A. Halbritter, M. Calame, *Nanoscale* **2017**, *9*, 17312.

[23] C. Nef, L. Pósa, P. Makk, W. Fu, A. Halbritter, C. Schönenberger, M. Calame, *Nanoscale* **2014**, *6*, 7249.

[24] M. Y. Han, J. C. Brant, P. Kim, *Phys. Rev. Lett.* **2010**, *104*, 056801.

[25] X. Wang, Y. Ouyang, L. Jiao, H. Wang, L. Xie, J. Wu, J. Guo, H. Dai, *Nat. Nanotechnol.* **2011**, *6*, 563.

[26] J. A. Mol, C. S. Lau, W. J. Lewis, H. Sadeghi, C. Roche, A. Cnossen, J. H. Warner, C. J. Lambert, H. L. Anderson, G. A. D. Briggs, *Nanoscale* **2015**, *7*, 13181.

[27] P. Giannozzi, O. Andreussi, T. Brumme, O. Bunau, M. B. Nardelli, M. Calandra, R. Car, C. Cavazzoni, D Ceresoli, M. Cococcioni, N. Colonna, I. Carnimeo, A. D. Corso, S. de Gironcoli, P. Delugas, R. A. D. Jr, A Ferretti, A. Floris, G. Fratesi, G. Fugallo, R. Gebauer, U. Gerstmann, F. Giustino, T. Gorni, J. Jia, M. Kawamura, H-Y Ko, A. Kokalj, E. Küçükbenli, M. Lazzeri, M. Marsili, N. Marzari, F. Mauri, N. L. Nguyen, H.-V. Nguyen, A Otero-de-la-Roza, L. Paulatto, S. Poncé, D. Rocca, R. Sabatini, B. Santra, M. Schlipf, A. P. Seitsonen, A. Smogunov, I Timrov, T. Thonhauser, P. Umari, N. Vast, X. Wu, S. Baroni, *J. Phys. Condens. Matter* **2017**, *29*, 465901.

[28] J. P. Perdew, K. Burke, M. Ernzerhof, *Phys. Rev. Lett.* **1996**, *77*, 3865.

[29] G. Prandini, A. Marrazzo, I. E. Castelli, N. Mounet, N. Marzari, *Npj Comput. Mater.* **2018**, *4*, 72.

[30] G. Pizzi, A. Cepellotti, R. Sabatini, N. Marzari, B. Kozinsky, *Comput. Mater. Sci.* **2016**, *111*, 218.

[31] J. Hutter, M. Iannuzzi, F. Schiffmann, J. Vandevondele, *Wiley Interdiscip. Rev. Comput. Mol. Sci.* **2014**, *4*, 15.

[32] J. VandeVondele, J. Hutter, *J. Chem. Phys.* **2007**, *127*, 114105.

[33] S. Goedecker, M. Teter, J. Hutter, *Phys. Rev. B* **1996**, *54*, 1703.

[34] I. Horcas, R. Fernández, J. M. Gómez-Rodríguez, J. Colchero, J. Gómez-Herrero, A. M. Baro, *Rev. Sci. Instrum.* **2007**, *78*, 013705.

[35] J. Overbeck, G. B. Barin, C. Daniels, M. Perrin, L. Liang, O. Braun, R. Darawish, B. Burkhardt, T. Dumslaff, X. Wang, A. Narita, K. Mullen, V. Meunier, R. Fasel, M. Calame, P. Ruffieux, *arXiv:1907.01797* **n.d.**

[36] A. Togo, I. Tanaka, *Scr. Mater.* **2015**, *108*, 1.

[37] G. Kresse, J. Furthmüller, *Phys. Rev. B* **1996**, *54*, 11169.

[38] G. Kresse, J. Furthmüller, *Comput. Mater. Sci.* **1996**, *6*, 15.

[39] G. Kresse, J. Hafner, *Phys. Rev. B* **1993**, *47*, 558.

[40] G. Kresse, D. Joubert, *Phys. Rev. B* **1999**, *59*, 1758.

[41] L. Liang, V. Meunier, *Nanoscale* **2014**, *6*, 5394.

[42] M. Gajdoš, K. Hummer, G. Kresse, J. Furthmüller, F. Bechstedt, *Phys. Rev. B* **2006**, *73*, 045112.

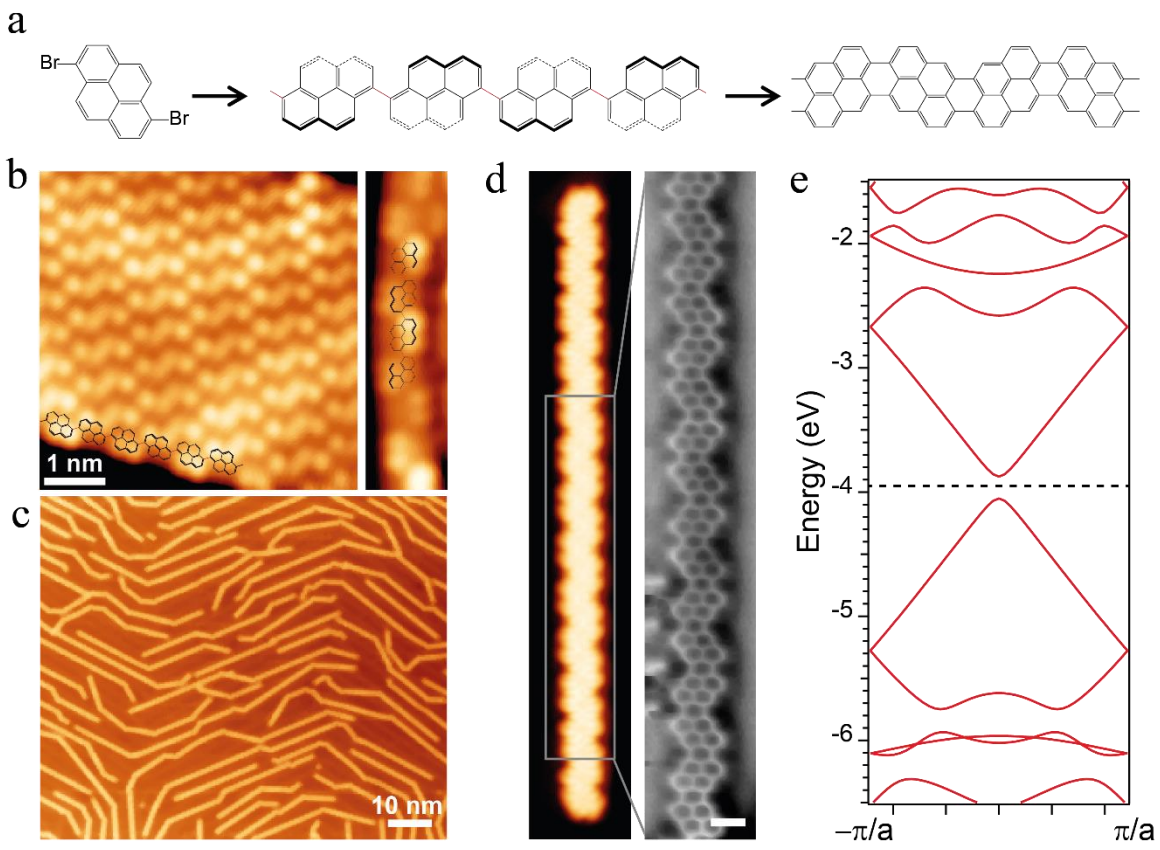

Figure 1. On-surface synthesis of the pyrene-based GNR (pGNR). **a,** Schematic representation of the on-surface synthesis route from a molecular precursor over a polymer phase to the pGNR. The structure of the intermediate polymer is nonplanar due to steric hindrance between neighboring pyrene units. **b,** STM images of the polymer phase on Au(111) (V_s = -1 V, I_t = 50 pA). **c**, STM image of the pGNR obtained after annealing the polymer to 300 ºC (V_s = -1 V, I_t = 50 pA). **d,** The high-resolution STM image of a pGNR (left panel, V_s = -0.2 V, I_t = 120 pA) and the nc-AFM image of the area indicated by the green rectangle (right panel, V_s = 5 mV, oscillation amplitude: ~80 pm). **e,** DFT-calculated band structure of the pGNR, energy is given with respect to the vacuum level.

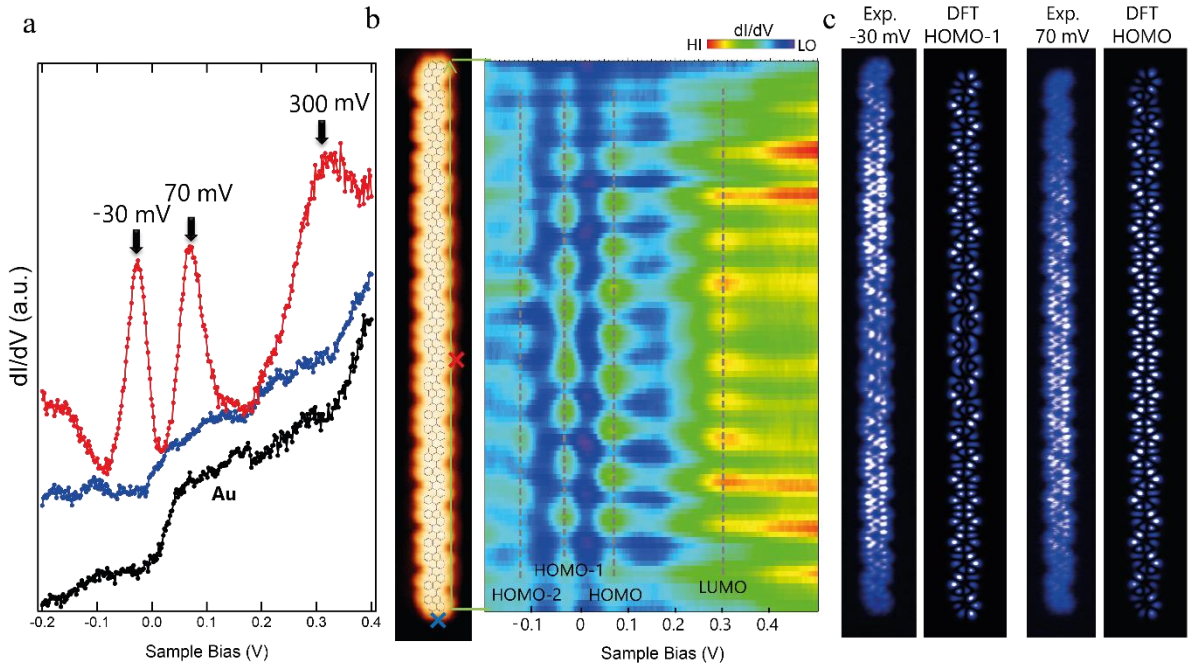

Figure 2. Electronic states of the pGNR. **a,** Differential conductance dI/dV spectra taken at the positions indicated by the crosses in the STM image in panel **b**. The spectra are vertically offset for clarity. The black curve is taken on a bare Au(111) for reference. **b,** STM image of the investigated pGNR (left), and color-coded map of the dI/dV spectra (right) taken along the green line shown in the STM image. Four clearly visible states are highlighted by dashed lines and assigned to their corresponding molecular orbitals. **c,** Constant-height dI/dV maps acquired at -30 mV and 70 mV and the corresponding DFT-calculated LDOS maps.

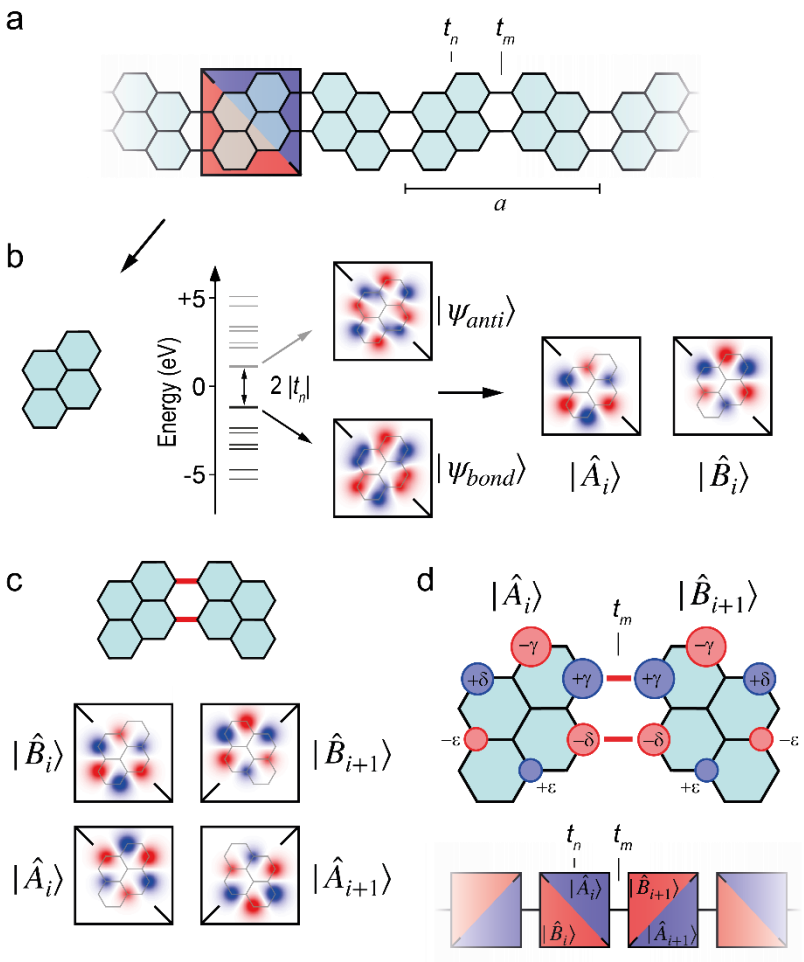

Figure 3. Conceptual illustration and model of the low bandgap pGNR. **a,** Structural model of the pGNR (top) shown with the relevant intramolecular (t_n) and intermolecular (t_m) coupling constants used in the SSH model. *a* is the unit cell length. **b,** Structural model of the pyrene unit shown with the low-lying electronic energy levels as derived from tight-binding (TB). The pyrene HOMO-LUMO gap is given by $2t_n$, where t_n is the intramolecular coupling constant. The decomposition of the HOMO ($|\Psi_{bond}\rangle$) and the LUMO ($|\Psi_{anti}\rangle$) into the A and B sub-lattice polarized zero-energy mode wave functions $|\hat{A}_i\rangle$ and $|\hat{B}_i\rangle$. **c,** Four state basis for two coupled pyrenes. **d,** Schematic representation of the coupling between two pyrenes with the amplitudes of the two coupling states.

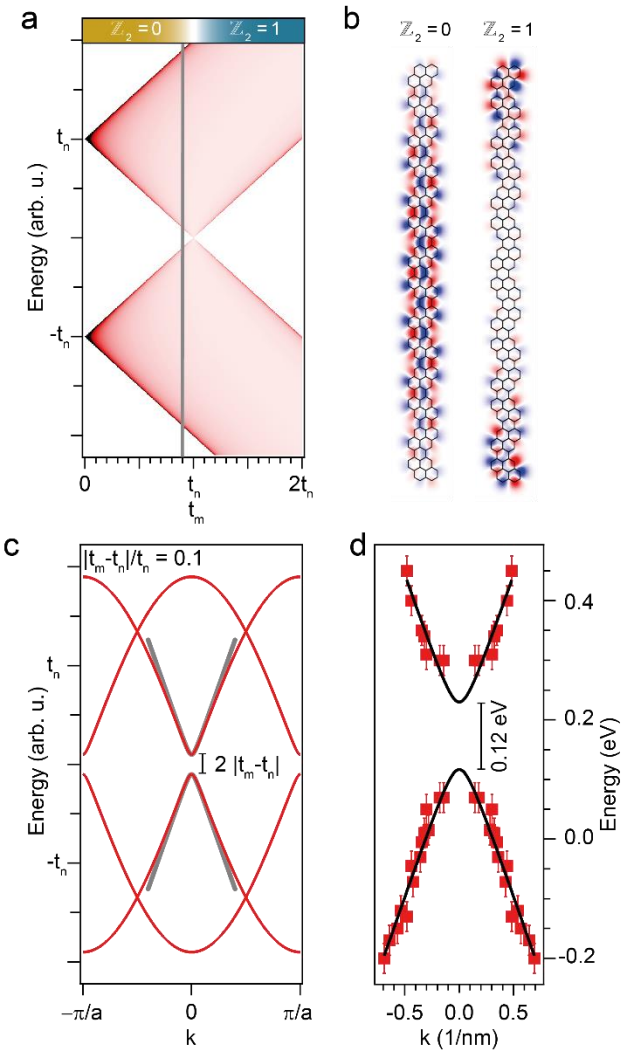

Figure 4. a, SSH-derived density of states (DOS) as a function of the intermolecular coupling constant t_m. The corresponding topological class is indicated by $\mathbb{Z}_2$. The grey dashed line marks the position $|t_m - t_n|/t_n = 0.1$. **b**, The TB-calculated HOMO wave functions of a finite-length pGNR belonging to topologically trivial ($\mathbb{Z}_2$ = 0) and non-trivial($\mathbb{Z}_2$ = 1) GNR, with t_m = 1/3t_n and t_m = 5/3t_n, respectively. **c**, Band dispersion of SSH-derived bands in the limit of small differences between intramolecular and intermolecular coupling constants ($|t_m - t_n|/t_n = 0.1$, red) shown together with the dispersion of massive Dirac fermions (Equation 6, $|\delta t|/t = 0.1$, grey). The resulting bandgap has a magnitude of 2|δt|. **d,** Plot of the experimental dispersions of VB and CB of the pGNR based on length-dependent energy position of the frontier states (red squares) using $k = \pm p\pi/\big((N+1)a\big)$. The black curve is a fit to the experimental data using the dispersion relation of massive Dirac fermions (Equation 7).

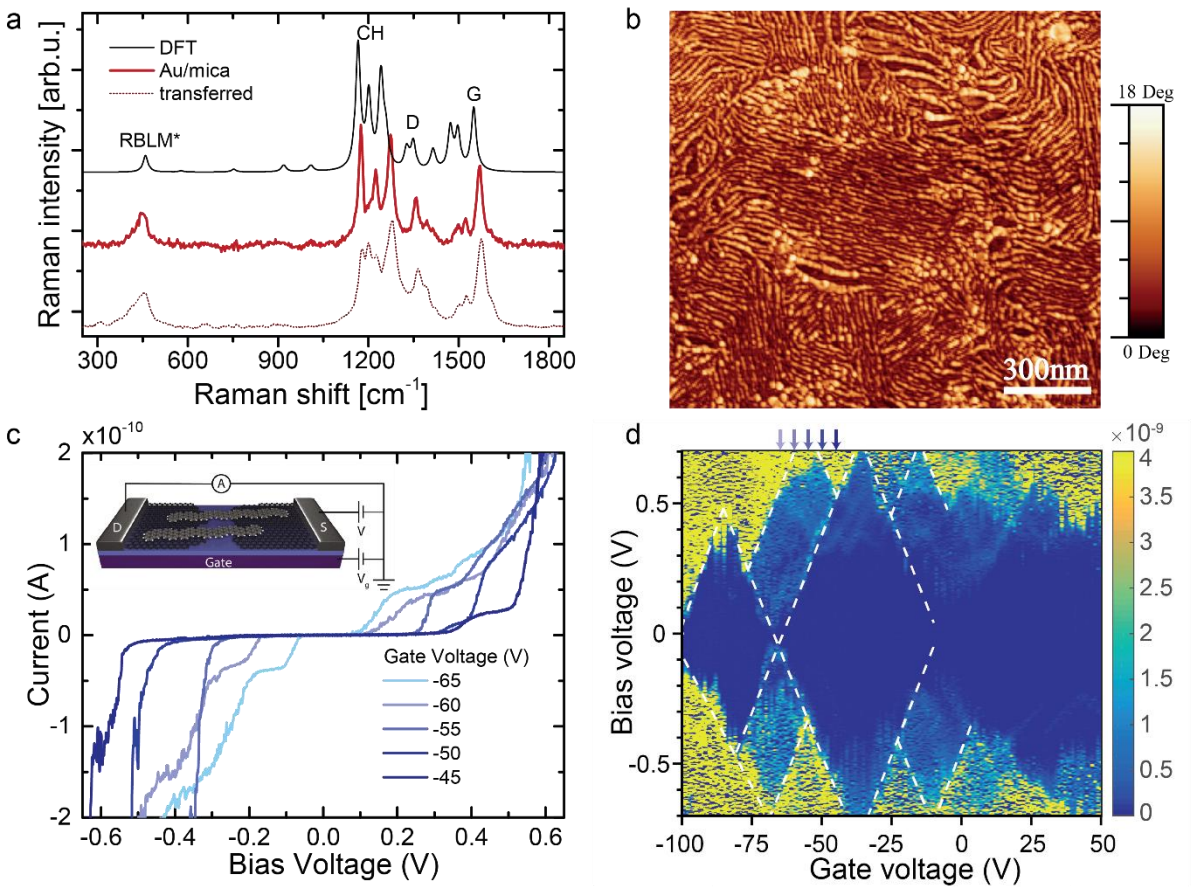

Figure 5. Ex-situ characterization of pGNR films and pGNR device characterization. **a,** Raman spectra of pGNR (top) simulated by DFT, (middle) acquired directly on the Au/Mica growth substrate, (bottom) and after substrate transfer to device substrates. Spectra are scaled to the same G-peak intensity. Excitation wavelength λ = 785 nm. Normal mode displacements corresponding to the labeled peaks are illustrated in Figure S11. **b,** AFM topography image of pGNRs transferred onto an Al_2O_3 substrate. **c,** Current-voltage traces at various gate voltages for a typical device recorded at 9K. The gate voltages at which these curves were recorded are marked with arrows in panel d. The inset shows the schematic of the device and measurement layout. **d,** dI/dV-map of the device in **c** as a function of applied bias and gate voltages. White dashed lines are guides to the eye

A new ultra-low bandgap GNR consisting of covalently fused pyrene subunits has been realized, whose charge carriers behave like massive Dirac fermions. The origin of the low bandgap derives from the periodically arranged molecular states of the pyrene units being in the limit of comparable intra- and inter- SSH-dimer coupling and can be rationalized by the SSH model.

Keyword: graphene nanoribbon, topological materials, scanning tunneling microscopy and spectroscopy, electronic structure

Q. Sun, O. Gröning, J. Overbeck, O. Braun, M. L. Perrin, G. B. Barin, M. El Abbassi, K. Eimre, E. Ditler, C. Daniels, V. Meunier, C. A. Pignedoli, M. Calame, R. Fasel, P. Ruffieux*

Massive Dirac fermion behavior in a low bandgap graphene nanoribbon near a topological phase boundary

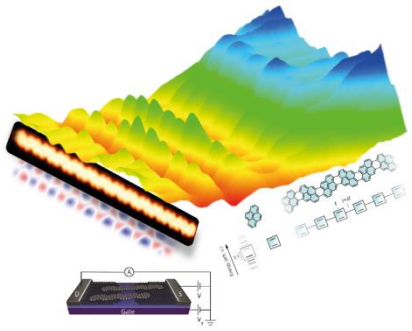

Supporting Information

Massive Dirac fermion behavior in a low bandgap graphene nanoribbon near a topological phase boundary

Qiang Sun, Oliver Gröning, Jan Overbeck, Oliver Braun, Mickael L. Perrin, Gabriela Borin Barin, Maria El Abbassi, Kristjan Eimre, Edward Ditler, Colin Daniels, Vincent Meunier, Carlo A. Pignedoli, Michel Calame, Roman Fasel, Pascal Ruffieux[*]

Contents

1. On-surface synthesis of the pyrene-based GNR (pGNR)

After deposition of the molecular precursor 1,6-dibromopyrene on Au(111) at room temperature, a self-assembled porous structure is observed, which is stabilized by halogen bonds as seen in the STM images (Fig. S1 a,c). For the polymer phase obtained upon annealing to 180 ºC, closely packed island structures are observed (Fig. S1 b,d), which are probably stabilized by π-π interaction between neighboring polymer chains due to the out-of-plane tilting of the pyrene units. Partial cyclodehydrogenation of the polymers is already observed at this temperate, resulting in planar pGNRs that are imaged with lower apparent height in STM (Fig. S1b). This indicates a lower cyclodehydrogenation threshold temperature than most other GNR systems, but well in line with the case of the (3,1)-chGNR which has a strained configuration in its polymer phase.[1] Also note that we did not observe the formation of organometallic intermediates like in the case for the formation of 5AGNR from dibromoperylene.[2]

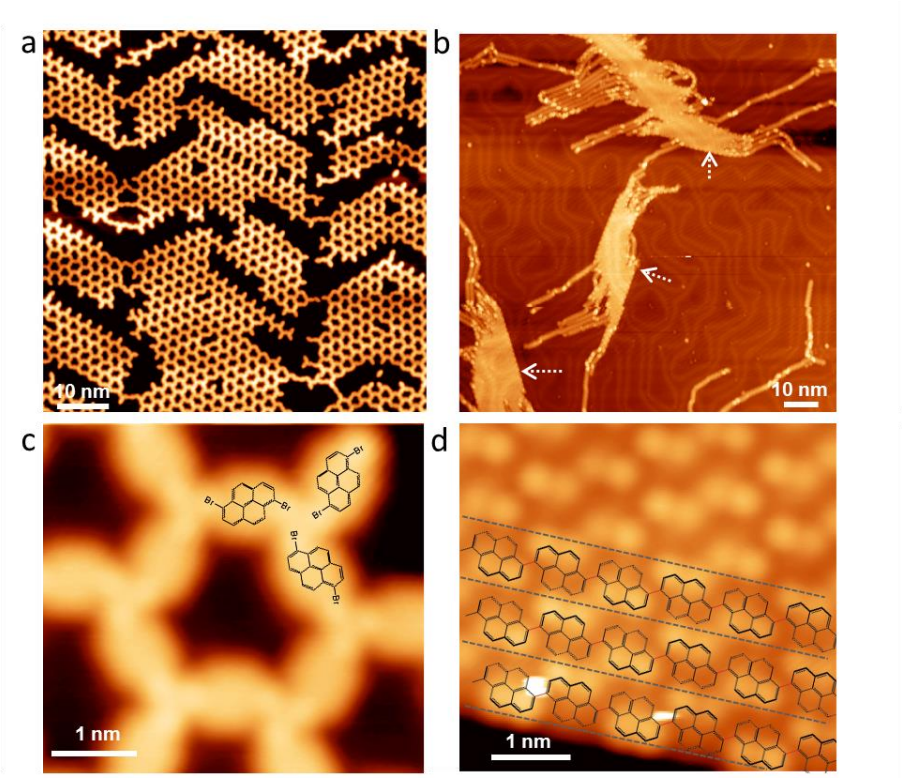

Supplementary Figure S1. Room-temperature and polymer phases. a. Large-scale and **c.** close-up STM images of the room-temperature phase on Au(111) (**a.** V_s = -1 V, I_t = 50 pA; **b**. V_s = -5 mV, I_t = 250 pA;). **b.** Large-scale and **d.** close-up STM images after annealing the sample to 180 ºC, where most of the molecules form island structures indicated by white arrows(**c**. V_s = -1 V, I_t = 50 pA; **d.** V_s = -20 mV, I_t = 200 pA). The polymers are identified by superimposing structural models to the STM image.

2. Reaction pathway

To investigate the reaction mechanism transforming the pyrene-based polymer into the pGNR, we use the nudged elastic band method in the climbing image formulation (NEB).[3] To avoid artifacts due to size limitations we adopted a large atomistic model with more than 1700 atoms. A polymer formed by six pyrene units is adsorbed on a Au(111) slab whose 2D periodic cell is 58.9 * 40.8 $Å^2$ in size. The slab contains four layers of Au. A layer of hydrogen atoms is added to one side of the slab to quench the Au(111) surface state. The hydrogen layer and the bottom two Au layers are kept fixed to ideal positions,

while all the other atoms are relaxed according to the optimization algorithm employed (for both geometry optimization and NEB).

All calculations are performed within density functional theory as implemented in the CP2K code[4]. Goedecker-Teter-Hutter pseudopotentials[5] are employed to represent the ionic potential, DZVP/TZV2P basis sets are employed for the Au/C,H species and a cutoff of 600 Ry is used for the plane wave expansion of the charge density. To account for van der Waals interactions we use the scheme proposed by Grimme.[6] Calculations were done within the AiiDA platform[7]. Due to the complexity of atomic rearrangements involved in the reaction, we do not rely on a direct linear interpolation between the geometries of initial and final states to create an initial guess for the reaction path. A chain of constrained geometry optimizations is performed for each reaction step where a collective variable (CV) (for example a C-C distance or the rotation angle of a pyrene unit) is forced to vary bringing the system from an initial to a final configuration. From the initial path thus created, we select an adequate number of images to perform the NEB calculations.

The reaction pathway that emerges from the simulation consists of six reaction steps as depicted in Fig. S2:

i) A pyrene unit within a segment of polymer (configuration 1) rotates reaching configuration 2. This step is dominated by an energy loss due to a reduction of van der Waals energy between the pyrene unit and substrate. However, the derived energy barrier of 1.73 eV suffers from an overestimation of vdW interaction typical of the Grimme approach. A more accurate approach[8–10], unfortunately still not implemented within CP2K, would result in a weaker interaction[11] and a lower barrier.

ii) Two carbon atoms (red spheres in Fig. S2) initially in a sp^2-hybridization state come closer to each other, followed by re-hybridizing to sp^3 carbons to accommodate the formation of a new C-C covalent bond. In this state, the hydrogen atoms (violet and cyan spheres) point towards and away from the surface respectively, yielding a tetrahedral geometry of the bonds of each carbon atom (configuration 3, energy barrier 1.44 eV).

iii) The H atom pointing toward the substrate (violet sphere) migrates toward the periphery of the ribbon (configuration 4, negligible energy barrier 0.03 eV).

iv) The H atom detaches and migrates to the Au surface (configuration 5, an energy barrier of 1.5 eV) where it starts diffusing and eventually desorbs from the substrate. We point out that a number of different paths for the dissociation of the C-H bonds can occur in reality according to the actual position of the polymer with respect to the surface gold atoms. The polymer is indeed expected to move on the substrate "slowly" compared to the dissociation events we are investigating, and thus, a number of paths with slightly different barriers have to be expected. Our aim here is to identify at least one path whose activation energy is compatible with the experimental conditions.

v) The H atom that is pointing away from the substrate (cyan sphere) migrates to the closest edge carbon atom (configuration 6, energy barrier 0.45 eV), which also occurs in the case of 7-AGNRs[12]. This grants a gain in dispersive energy since the overall geometry becomes flatter. A direct dissociation to the vacuum region would have a high energy barrier and is unlikely to happen.

vi) After migration, the H atom can further detach from the structure upon a C-H bond cleavage (configuration 7, energy barrier 0.46 eV). The H atom corresponding to the green sphere is in this case the H closest to the substrate.

We note that our NEB calculations depict the energy profile of the system at 0K along a possible minimum energy reaction pathway. As such, energy presented in the graph corresponds to enthalpy and does not include entropic effects. Also note that the current calculation does not consider the desorption of H atoms into the vacuum, which can correspond to an energy gain of 1eV for one H in

such systems.[13] We have drawn additional dashed lines in Fig. S2a to indicate the effect of the H desorption (step 5, 6 and 7).

We also note that we did not observe the intermediate 4 in experiments. Despite this state being characterized by a very low enthalpy, it is quite unlikely to observe such a state in the experiment. This state is reached when a H atom detached from C (starting geometry 3) migrates over the substrate, and instead of abandoning the polymer it attaches again to a different C atom (step 4). This low energy configuration (intermediate 4) is quite unlikely to occur since it requires a specific orientation of the polymer with respect to the substrate, a very specific path of H migration on the substrate and the additional condition that no other H atoms diffusing on the substrate would recombine with this particular H atom. We included this state in our diagram for completeness, to grant the reproducibility of our results and to highlight that despite this state is low in energy, the barrier to escape from it can still be overcome at the experimental temperature used to trigger the initial steps of the reaction.

To indicate the most likely reaction path that would not step through intermediate 4, we added a dashed line bridging state 3 and state 5 In Figure S2,.

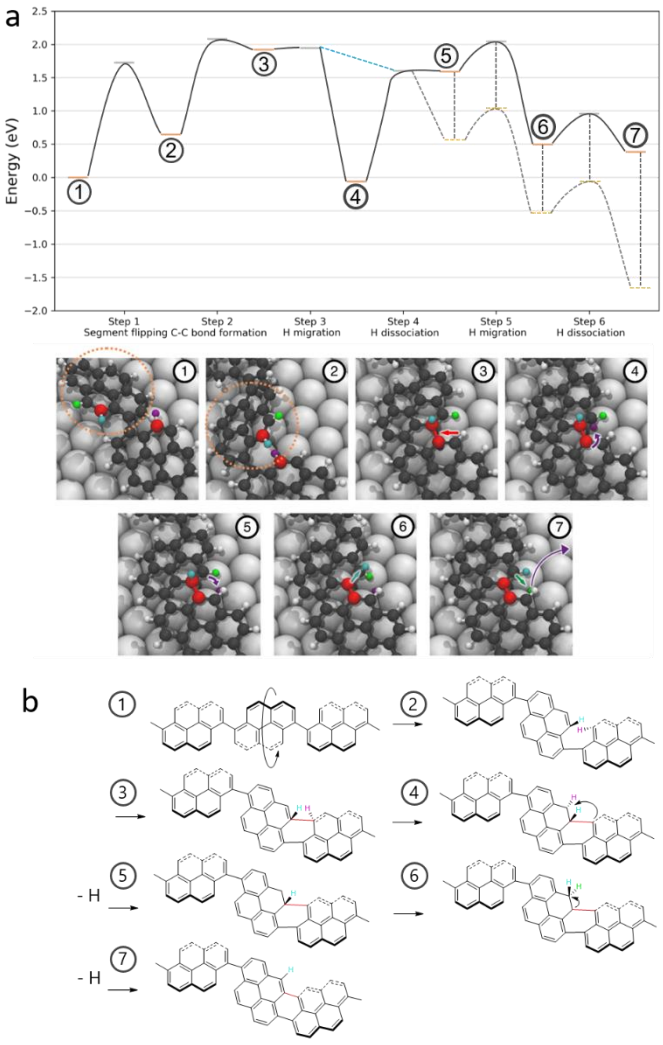

Supplementary Figure S2. Reaction pathway to fuse one segment of the polymer into a planar segment of pGNR. **a**. In the top panel, the activation barriers between the different metastable states are sketched with parabolas. An endothermic energy of 1eV is considered for one H atom desorption from the surface into vaccum in step 5, 6 and step 7, giving an additional energy profile indicated by

dashed curves. The blue line bridging state 3 and state 5 corresponds to the path most likely occurring in experiments. The lower panels are ball and stick representations of the corresponding atomistic models in each configuration labeled accordingly. The large spheres in light gray represent Au atoms. Small (white, cyan violet and green) spheres are H atoms. Dark grey and red spheres are C atoms. **b**. The corresponding reaction path described by chemical sketches.

3. Electronic properties of the pGNR

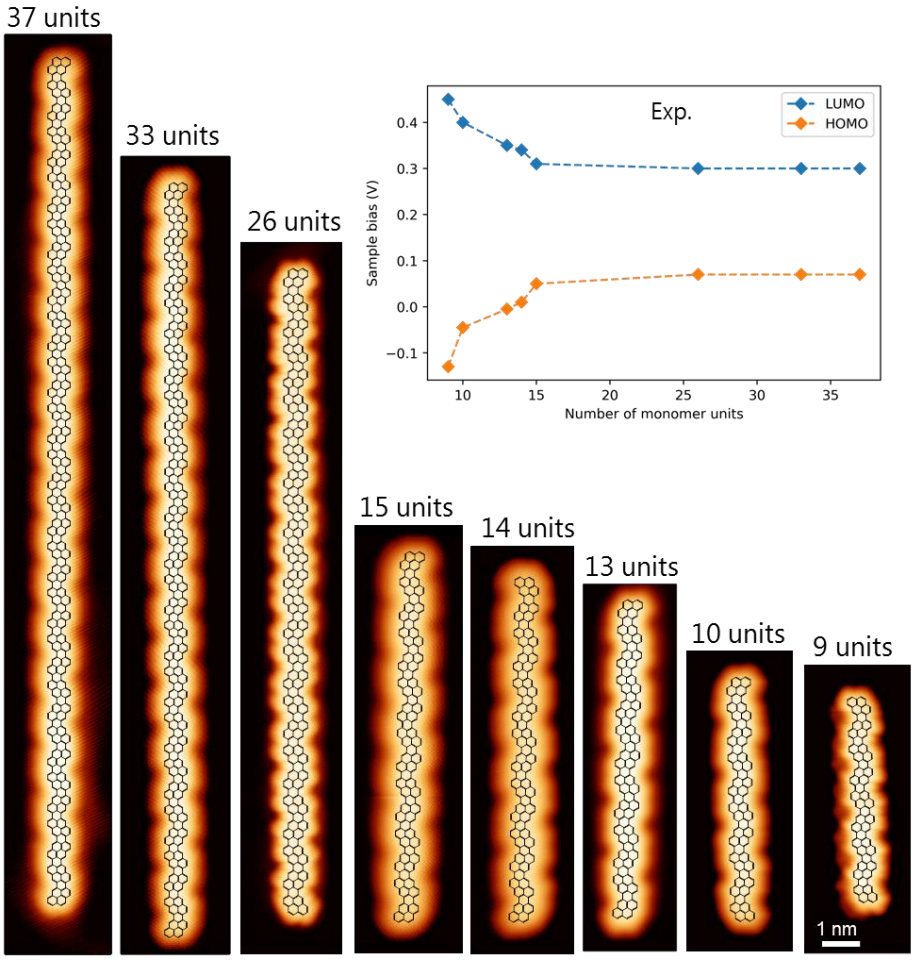

Supplementary Figure S3. STM images of pGNRs of different lengths, and the energy positions of their frontier states on Au(111) as determined by STS. It is seen that the electronic bandgap gap converges to 230 mV with increasing ribbon length.

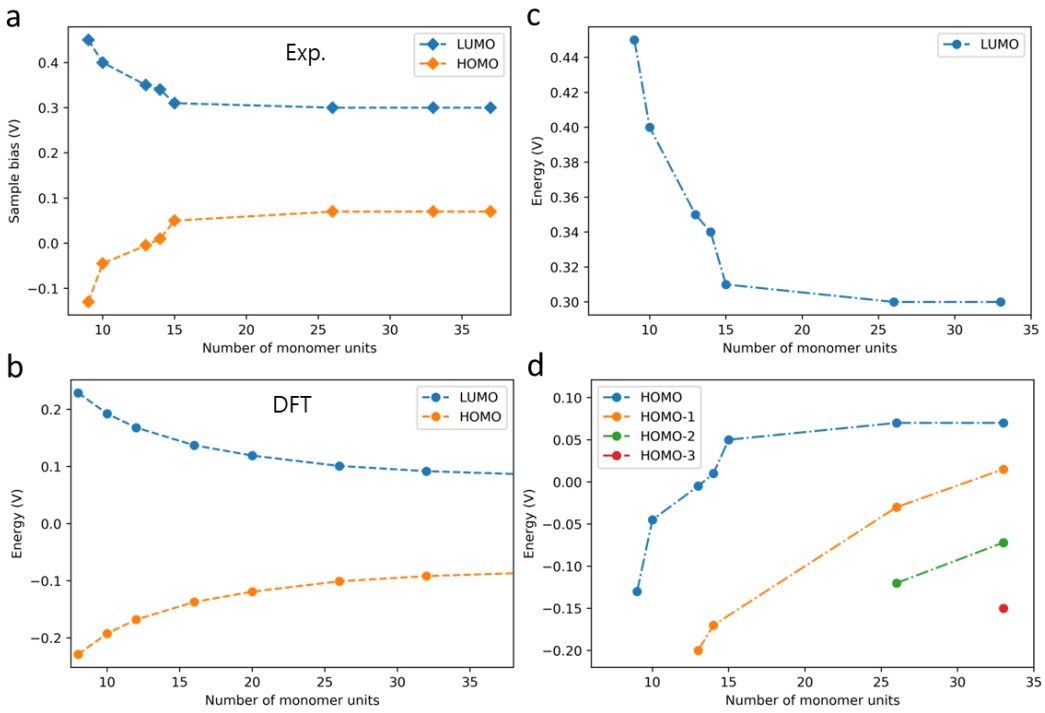

Supplementary Figure S4. **a, b,** The experimental and DFT calculated energy positions of frontier states of finite-length pGNRs as a function of length (in terms of constituting pyrene units). **c, d,** The experimental energy positions of the unoccupied and occupied orbitals as a function of pGNR length.

Determination of the band dispersion from frontier orbital energy positions:

The band dispersions of pGNR in Fig. 3e are determined from the finite-length frontier orbital energy positions of pGNRs (data points in Fig. S4 c,d). For a 1D quantum well, the wave functions Ψ_p of the system are sinusoids with discrete wave vectors $\mathrm{k} = \pm \mathrm{p}\pi/\mathrm{L}$ and a number of discrete energy levels E_p[14], where *p* is the order of the confined frontier states. The energy levels E_p can be determined by differential conductance dI/dV spectroscopy, which probes the local density of states that is proportional to the square of the wave ${\Psi_p}^2$. By plotting the frontier energy positions of finite-length pGNRs as a function of their corresponding wave vectors, one can thus determine the dispersion of their frontier bands.

For the width of the quantum well confining the pGNR electronic states, we use the effective length $\mathrm{L} = (N+1)\mathrm{a}$ of the pGNR, where *N* is the number of the repeating molecular units and *a* is the length of the unit cell. The extension by 1 molecular unit takes into account that the wave function envelope of the frontier orbitals will go to zero not at the structural extremities of the finite ribbon, but at the center of the virtual neighboring unit cell. Generally, the effective length to be considered for the correct description of the allowed wave vectors in finite GNRs critically depends on the atomic configuration at the GNR termini[15]. Here, by numerical simulations of the periodic pGNR and finite systems with varying N, we find $\mathrm{k(N)} = \pm \mathrm{p}\pi/((\mathrm{N}+1) * \mathrm{a})$ to be an adequate mapping function of the chain length to the equivalent wave vector.

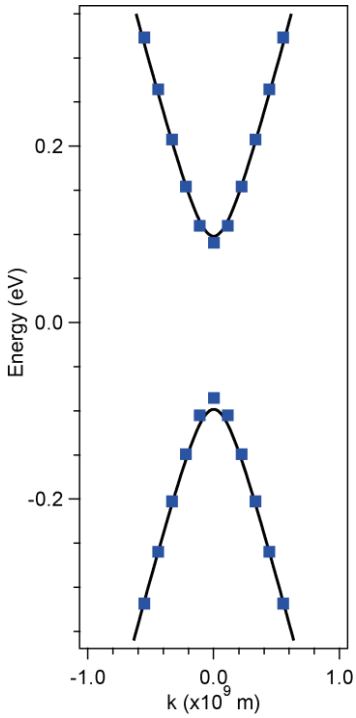

Supplementary Figure S5. The DFT calculated valence and conduction band dispersion of pGNR (blue squares) fit by the dispersion relation of massive Dirac fermions (black curves). The effective mass derived from the fit is 0.025 m_e, where m_e is the electron rest mass. The fit is done by considering both VB and CB simultaneously and with equal parameters δt and t.

4. Construction of the SSH model for the pGNR

In order to describe the frontier bands of the pGNR within the SSH model, i.e. in terms of a dimerized chain of electronic states, we need to deconstruct the electronic structure of the pGNR around the Fermi level.

Before doing so, we briefly reiterate the construction of the valence and conduction band in the SSH model from the two uncoupled basis states $|\hat{A}_i\rangle$ and $|\hat{B}_i\rangle$ which constitute the dimer. This process is represented schematically in Fig. S6. Starting from the left we can see how 'switching on' the intra- SSH-dimer coupling (i.e. going from $t_n = 0$ to $t_n \neq 0$) leads to hybridization of the two zero-energy basis states $|\hat{A}_i\rangle$ and $|\hat{B}_i\rangle$ to the bonding and anti-bonding states $|\psi_{bond}\rangle$ and $|\psi_{anti}\rangle$ of the SSH-dimer, with an energy splitting that corresponds to twice the absolute value of the coupling term $t_n = \langle\hat{A}_i|H_n|\hat{B}_i\rangle$, where H_n denotes the intra- SSH-dimer coupling term of the Hamiltonian. We note that $|\psi_{bond}\rangle$and $|\psi_{anti}\rangle$ are nothing else than the HOMO and LUMO of the dimer, which will be important in the discussion further below. Coupling a periodic sequence of SSH-dimers (i.e. with an inter- SSH-dimer coupling $t_m \neq 0$) will then result in the formation of the valence and conduction bands with $t_m = \langle\hat{A}_i|H_m|\hat{B}_{i+1}\rangle$. Here, H_m denotes the inter- SSH-dimer coupling Hamiltonian, and the indices i and i+1 denote the i^{th} and $(i+1)^{th}$ dimer of the chain.

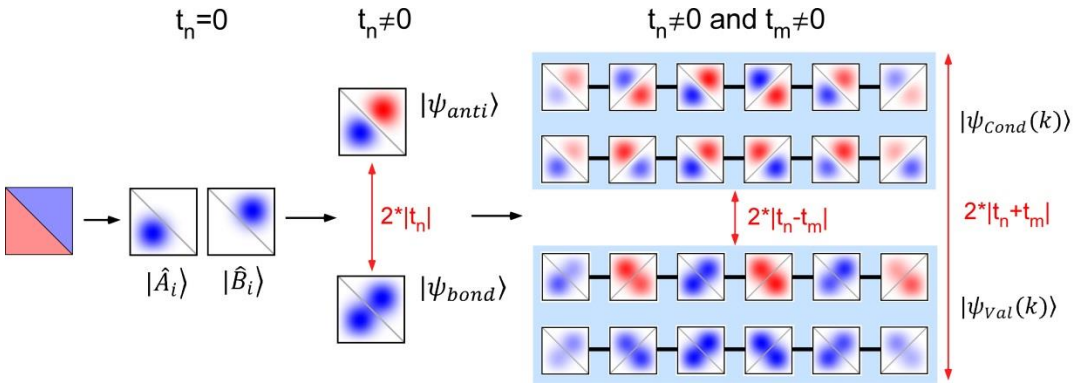

Supplementary Figure S6. Schematic representation of the construction of the SSH dimerized chain from the SSH-dimer building blocks on the left to the valence and conduction band states to the right. The dots in the squares symbolize the state amplitude and color symbolizes the parity, the vertical axis denotes energy.

The relations between $|\hat{A}_i\rangle$, $|\hat{B}_i\rangle$, $|\psi_{bond}\rangle$ and $|\psi_{anti}\rangle$ are evidently the following:

$$|\psi_{bond}\rangle = \frac{1}{\sqrt{2}}(|\hat{A}_i\rangle + |\hat{B}_i\rangle) \quad \text{and} \quad |\psi_{anti}\rangle = \frac{1}{\sqrt{2}}(|\hat{A}_i\rangle - |\hat{B}_i\rangle) \tag{1}$$

$$|\hat{A}_i\rangle = \frac{1}{\sqrt{2}}(|\psi_{bond}\rangle + |\psi_{anti}\rangle) \quad \text{and} \quad |\hat{B}_i\rangle = \frac{1}{\sqrt{2}}(|\psi_{bond}\rangle - |\psi_{anti}\rangle) \tag{2}$$

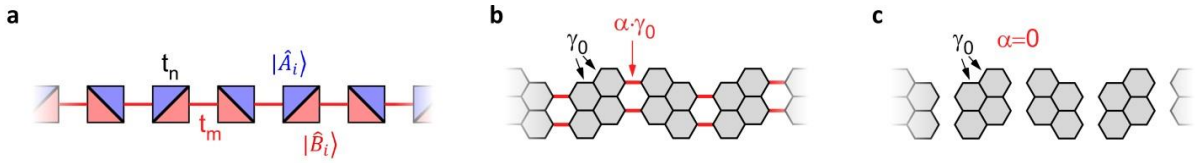

Supplementary Figure S7. **Relation between the two-level SSH chain and pGNR with variable pyrene-pyrene coupling. a.** Schematic representation of the SSH chain with the zero-energy modes $|\hat{A}_i\rangle$ and $|\hat{B}_i\rangle$ as basis. **b.** Tight Binding model of the coupled pyrene with variable pyrene-pyrene coupling parameter α. **c.** Schematic representation for α=0, i.e. the decoupled pyrene chain.

As discussed in the main text, representing the frontier bands of the pGNR would lead to a quasi-metallic band structure with a nearly vanishing gap (because $t_n \approx t_m$). This prediction can be compared with a TB calculation on the full pGNR structure (i.e. taking into account all 32 π-bands). Here, we keep the C $2p_z$ hopping parameter constant at γ_0 for all bonds within the pyrene unit (i.e. the intra- SSH-dimer coupling) but vary it for the bonds connecting the pyrenes (i.e. the inter- SSH-dimer coupling which we denote as $\gamma_{IP} = \alpha^*\gamma_0$) as shown in Fig. S7b. We now plot the density of states as a function of the inter- SSH-dimer coupling (α) in Fig. S8a. As can be seen the band gap progressively closes as γ_{IP} approaches γ_0 (i.e. α=1). The gap vanishes for $\gamma_{IP} = 1.16\gamma_0$ which is indicated by the red line in Fig. S8a, and the corresponding band structure is shown in Fig. S8c. The natural choice of $\gamma_{IP} = \gamma_0$ (black line in Fig. S8a and band structure shown in Fig. S8c) will yield a small bandgap and a winding number of 0 making this situation $\mathbb{Z}_2$=0 topologically trivial. For $\gamma_0 < \gamma_{IP} = 1.32\gamma_0$ (yellow line in Fig. S8a and band structure in Fig. S8d) we find a topologically non-trivial $\mathbb{Z}_2$ = 1 situation, revealing topological end states.

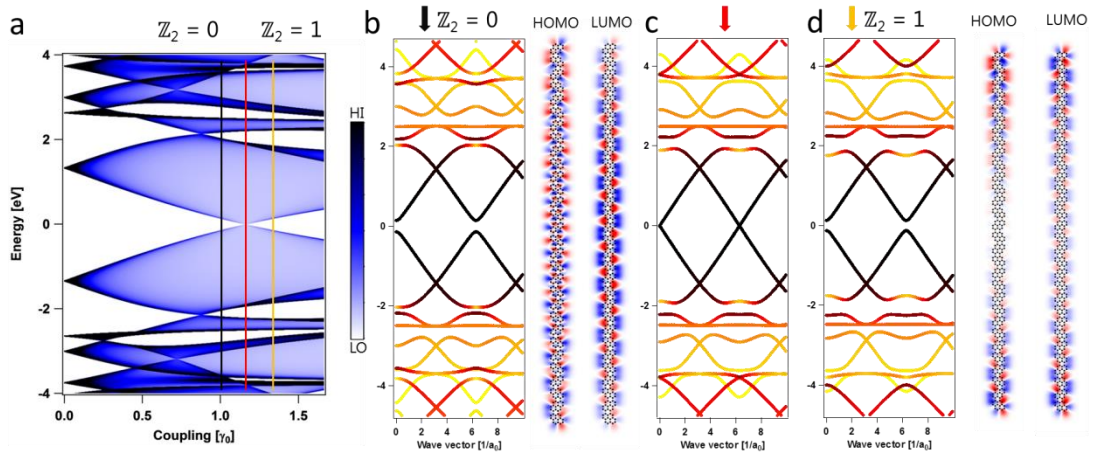

Supplementary Figure S8. **TB calculations regarding the topology of the pyrene ribbon. a.** Energy diagram of the pGNR as a function of the inter-pyrene coupling strength $\gamma_{IP} = \alpha^*\gamma_0$ while keeping the intra-pyrene coupling constant at γ_0. The red line in indicates the topological phase boundary at an inter-pyrene coupling strength of $\gamma_{IP} = 1.16\gamma_0$. **b.** Left: Band structure of the pGNR with a trivial electronic topology (at $\gamma_{IP} = \gamma_0$), which is indicated by the black arrow in **a**. Right: The wave functions of the HOMO and LUMO of a finite-length pGNR, where there are no topological end states. **c.** Band structure of the pGNR located at the topological phase boundary (at $\gamma_{IP} = 1.16\gamma_0$), which is indicated by the red arrow in **a**. **d.** Left: Band structure of the pGNR with a non-trivial topology (at $\gamma_{IP} = 1.32\gamma_0$), which is indicated by the yellow arrow in **a**. Right: The wave functions of its HOMO and LUMO of a finite-length pGNR, where the topological end states are clearly seen. The color (yellow = 0 to black = 1) in the band structures encodes the projection of the band states onto the dimer states according to $\rho_n(k) = \frac{1}{2}\{|\langle \hat{A}_i|\psi_n(k)\rangle| + |\langle \hat{B}_i|\psi_n(k)\rangle|\}$.

The fact that for the natural case α=1, i.e. $\gamma_{IP} = \gamma_0$ the full TB model of Fig. S8b yields a larger band gap than the two-level SSH model (see main text) is due to the non-linear closure of the gap shown in Fig. S8a for the full TB calculation. This non-linearity is due to the hybridization of the frontier bands of the pGNR with higher/lower orbitals than just the LUMO/HOMO of the pyrene. This is expressed in the values of $\rho_{CB}(\Gamma) = \rho_{VB}(\Gamma) = 0.933$ and $\rho_{CB}(\mathrm{X}) = \rho_{VB}(\mathrm{X}) = 0.874$ not being 1 for the valence and conduction band (VB and CB) at the G and X points of the Brillouin zone.

5. Raman characterization of pGNRs

Experimental details:

Raman spectra were acquired with a confocal Raman microscope (WITec Alpha 300R) before (on Au/mica) and after substrate transfer (on Al_2O_3/Au/SiO_2/Si) using 785 nm, 532 nm and 488 nm laser wavelengths. All Raman measurements were performed in vacuum (<10^{-2} mbar) using a 50 × objective with a numerical aperture NA = 0.55.

Raman spectra were acquired using a mapping approach and samples were transferred onto Raman-optimized-device type substrates with a top-layer of Al_2O_3.[16] We optimized the measurement settings for each sample-wavelength combination as summarized in Table T1.

In Fig. S9 we provide an example of signal-optimization and background subtraction.

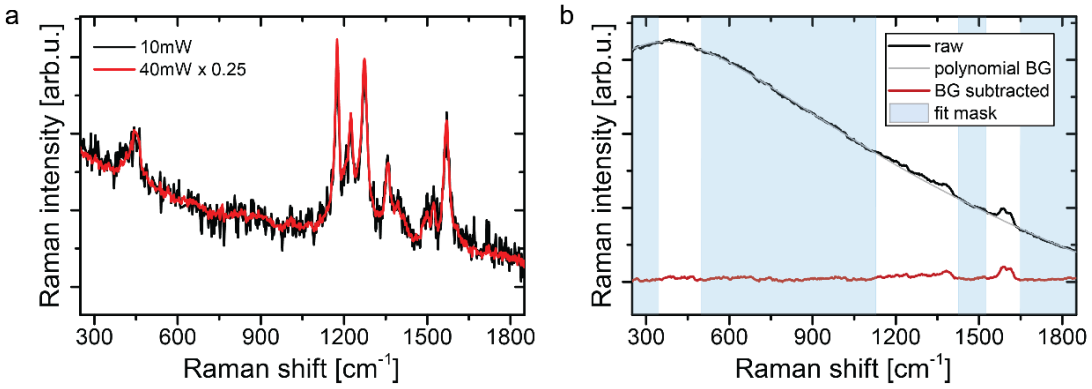

Supplementary Figure S9. Data acquisition and processing. a, Raw spectra of pGNRs on a Au/Mica substrate acquired with 785 nm excitation wavelength in vacuum for 10 mW and 40 mW excitation power. No power-dependent change is observed in the spectra. **b,** Example for data processing by polynomial background subtraction. A polynomial is fitted to the raw data with a fit mask excluding Raman lines, resulting in a spectrum with a flat baseline. This makes it easier to compare spectra acquired with different excitation wavelengths (which result in different backgrounds) and theory.

Supplementary Table T1. The optimized parameters for each of the spectra in Fig. 4a of the main text and Fig. S12. The scaling factor to allow for a comparison of signal-to-noise ratios is computed as follows: scaling factor = 1 / (power*integration-time*number$^{0.5}$).

Laser wavelength	Substrate	Power (mW)	Integration time (s)	Number of averaged spectra	Scaling factor
785 nm	Au/Mica	40	60	3	1/4157
	Al_2O_3	5	0.3	900	1/45
532 nm	Au/Mica	2	26	25	1/260
	Al_2O_3	2	0.3	900	1/18
488 nm	Au/Mica	20	3	400	1/1200
	Al_2O_3	0.5	1	3600	1/30

Normal mode analysis:

Fig. S10 shows the DFT-calculated Raman spectrum for an excitation energy of 2.54 eV (panel a) and the normal mode displacements (panel b) corresponding to the most intense modes. We display the

fundamental acoustic mode defined by the size of a pGNR unit cell in a plot showing four pyrene units to highlight its relation to the ribbon geometry.

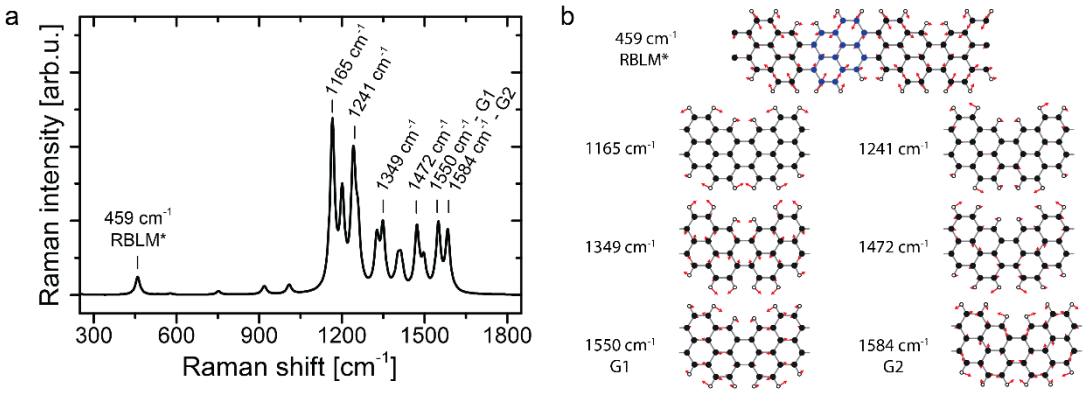

Supplementary Figure S10. pGNR normal mode analysis. a. DFT-calculated Raman spectrum for an excitation energy of 2.54 eV. **b.** Normal mode atomic displacements of the modes labelled in a. A single pyrene unit is highlighted in blue in the topmost structure

Wavelength dependent Raman spectra:

In addition to the spectrum shown in Fig. 5a of the main text, we also acquired Raman spectra at 532 nm and 488 nm excitation wavelength. These are displayed for comparison in Fig. S11 with a scaling factor applied to account for the different acquisition modes. The spectra after transfer are obtained on interference substrates optimized for excitation at 488 nm[16]. This allows the observation of additional features with visible light excitation, however the spectra acquired with infrared excitation remain the ones showing most details. Fig. S11b shows calculated Raman spectra for the same wavelengths. These reproduce the experimentally observed spectra remarkably well, in particular the relative intensity of LO and TO phonons that contribute to the G-like peak around 1600 cm^{-1}. While the non-resonant Raman cross-section should increase with the 4th power of photon energy, the spectrum acquired with 785 nm excitation shows the highest signal-to-noise ratio for acquisition directly on the growth substrate. Moreover, it is the only spectrum clearly exhibiting the low-energy geometry-dependent RBLM*. This points towards a resonance effect in the near infrared which agrees with the predicted narrow electronic bandgap as reflected in the higher intensity for the calculated Raman spectra at the 785 nm excitation.

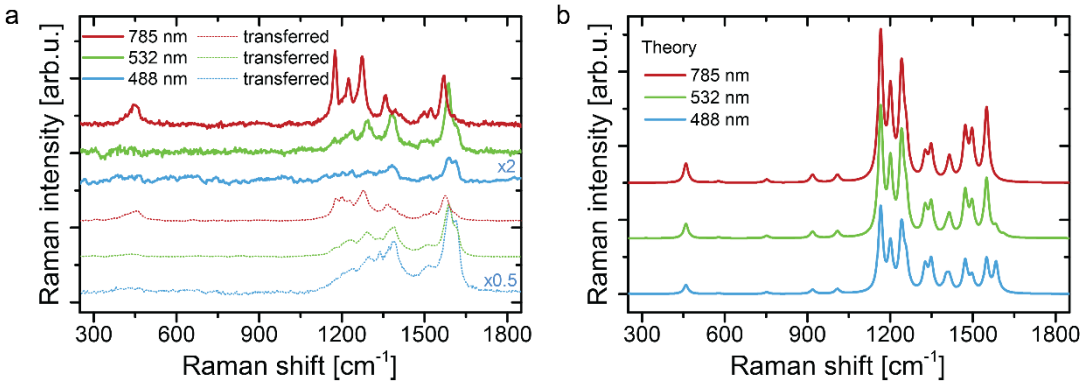

Supplementary Figure S11. Wavelength-dependent Raman spectra. a, pGNR Raman spectra obtained directly on the Au/Mica growth substrate (solid lines) and after substrate transfer to (interference optimized) device substrates. Spectra are offset for clarity and scaled with the factor mentioned in Table T1 (and an additional factor of 2 as noted in the figure). **b,** DFT-calculated wavelength-dependent Raman spectra.

6. Transport characterization of pGNRs

The electrical transport properties of pGNRs were characterized as described in the main manuscript and methods. Fig. S12 below shows additional measurements of the gap characteristics of the device discussed in Fig. 5c (Device 1) before and after ribbon substrate transfer. Fig. S13 shows low-temperature stability diagrams for two additional devices.

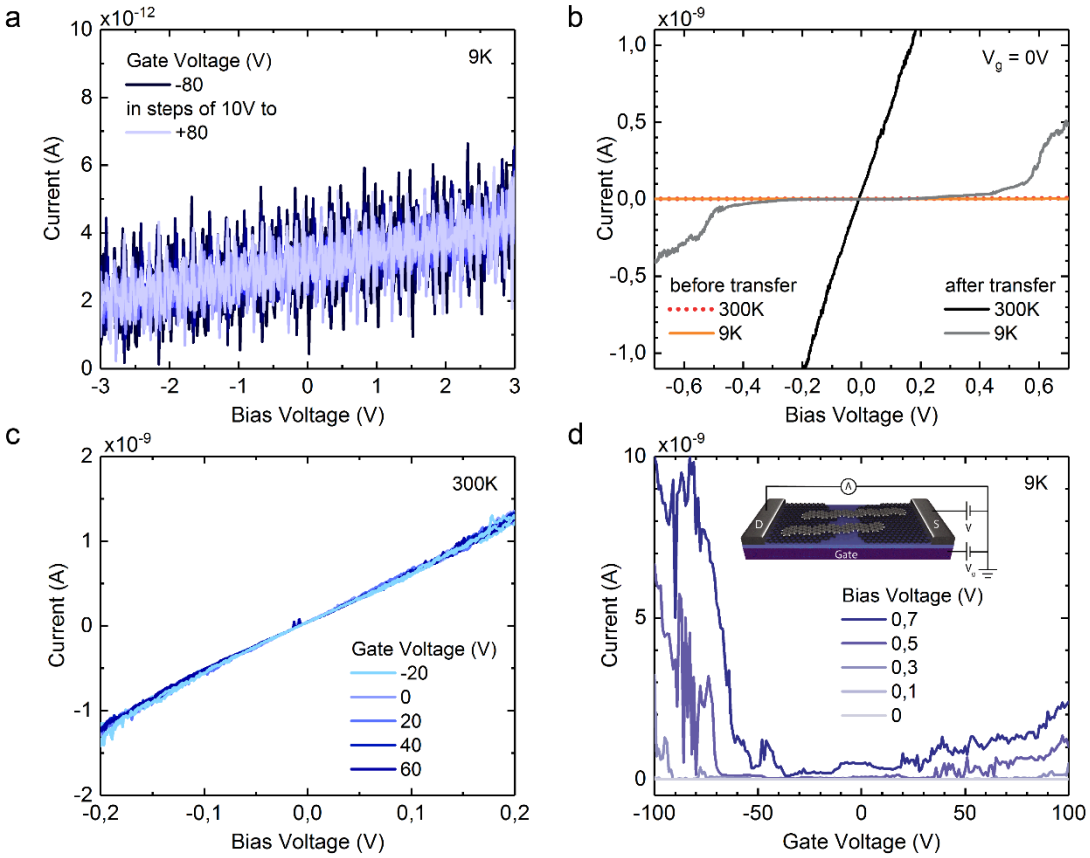

Supplementary Figure S12. **Additional electrical characterization of Device 1. a.** Electrical characterization of the gap after the electrical breakdown process at 9 K. Superimposed I-V characteristics recorded at gate voltages from -80 V to +80 V in steps of 10 V confirm an empty gap in all regimes. The noise-level is 2 pA with a current offset of 3 pA at V_{bias} = 0 V. **b.** Comparison of device performance before and after transfer of the pGNRs. **c.** Room temperature I-V characteristics at different gate voltages indicating no gate dependence. **d.** Source-drain current *vs* gate voltage at different bias voltages corresponding to horizontal cuts in Fig. 5d of the main manuscript. A maximum on current of 10 nA is measured at a bias voltage of 0.7 V.

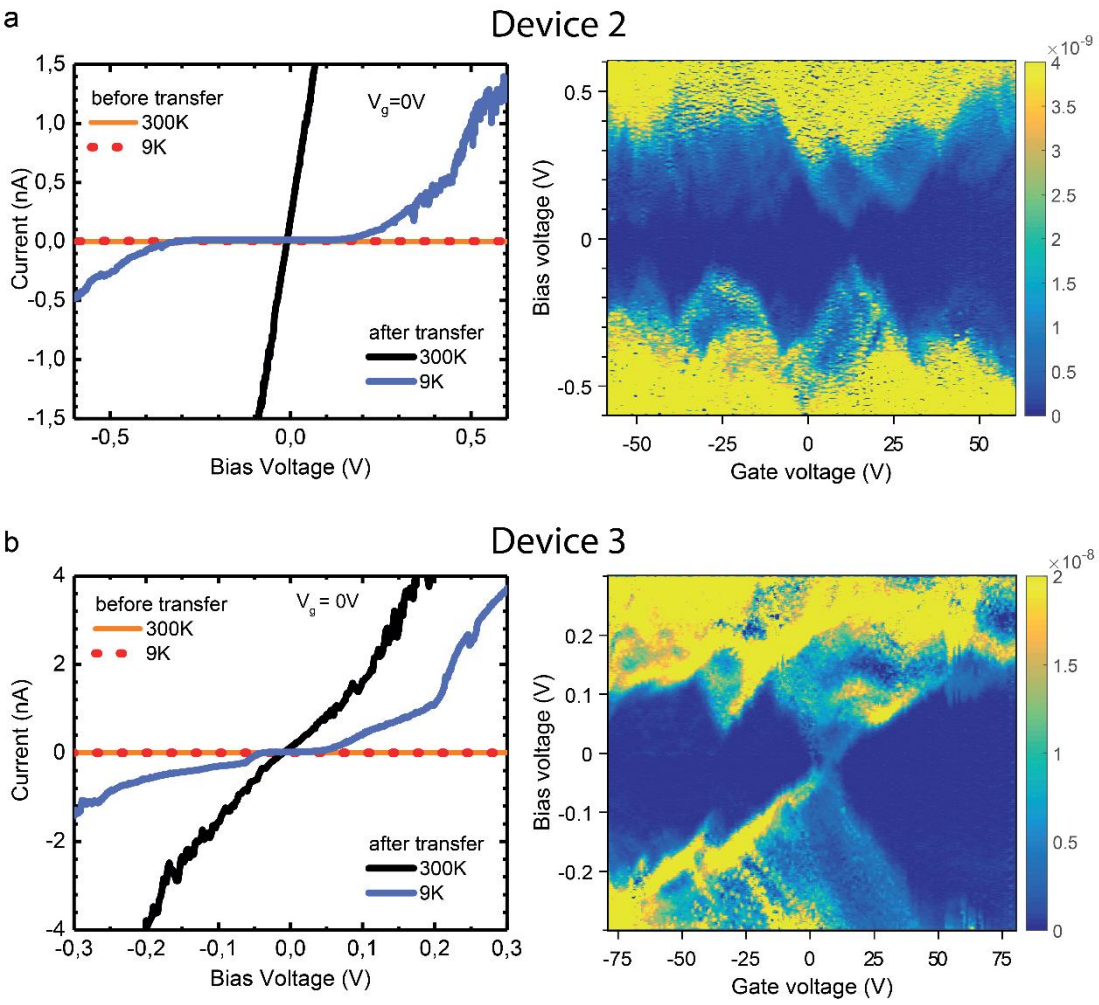

Supplementary Figure S13. **Electrical characterization of additional pGNR devices.** Electrical measurements recorded on **a.** Device 2, **b.** Device 3. Left panel: I-V characteristics before and after the incorporation of the pGNRs, measured at 9 K and 300 K, respectively. The I-V characteristics without pGNRs (labelled "before transfer") indicate an empty gap. Right panel: dI/dV-map of the corresponding pGNR device as a function of the applied bias voltage and gate voltage, recorded at 9 K.

7. References

[1] N. Merino-Díez, J. Li, A. Garcia-Lekue, G. Vasseur, M. Vilas-Varela, E. Carbonell-Sanromà, M. Corso, J. E. Ortega, D. Peña, J. I. Pascual, D. G. de Oteyza, *J. Phys. Chem. Lett.* **2018**, *9*, 25.

[2] K. Sun, P. Ji, J. Zhang, J. Wang, X. Li, X. Xu, H. Zhang, L. Chi, *Small* **2019**, *15*, 1804526.

[3] G. Henkelman, B. P. Uberuaga, H. Jónsson, *J. Chem. Phys.* **2000**, *113*, 9901.

[4] J. Hutter, M. Iannuzzi, F. Schiffmann, J. VandeVondele, *Wiley Interdiscip. Rev. Comput. Mol. Sci.* **2014**, *4*, 15.

[5] S. Goedecker, M. Teter, J. Hutter, *Phys. Rev. B* **1996**, *54*, 1703.

[6] S. Grimme, J. Antony, S. Ehrlich, H. Krieg, *J. Chem. Phys.* **2010**, *132*, 154104.

[7] G. Pizzi, A. Cepellotti, R. Sabatini, N. Marzari, B. Kozinsky, *Comput. Mater. Sci.* **2016**, *111*, 218.

[8] V. G. Ruiz, W. Liu, E. Zojer, M. Scheffler, A. Tkatchenko, *Phys. Rev. Lett.* **2012**, *108*, 146103.

[9] A. Tkatchenko, R. A. DiStasio, R. Car, M. Scheffler, *Phys. Rev. Lett.* **2012**, *108*, 236402.

[10] A. Ambrosetti, A. M. Reilly, R. A. DiStasio, A. Tkatchenko, *J. Chem. Phys.* **2014**, *140*, 18A508.

[11] A. V. Yakutovich, J. Hoja, D. Passerone, A. Tkatchenko, C. A. Pignedoli, *J. Am. Chem. Soc.* **2017**, DOI 10.1021/jacs.7b10980.

[12] S. Blankenburg, J. Cai, P. Ruffieux, R. Jaafar, D. Passerone, X. Feng, K. Müllen, R. Fasel, C. A. Pignedoli, *ACS Nano* **2012**, *6*, 2020.
[13] J. Bjo�rk, *J. Phys. Chem. C* **2016**, *120*, 21716.
[14] C. Kittel, P. McEuen, *Introduction to Solid State Physics*, Wiley New York, **1976**.
[15] L. Talirz, H. Söde, S. Kawai, P. Ruffieux, E. Meyer, X. Feng, K. Müllen, R. Fasel, C. A. Pignedoli, D. Passerone, *ChemPhysChem* **2019**, *20*, 2348.
[16] J. Overbeck, G. B. Barin, C. Daniels, M. Perrin, L. Liang, O. Braun, R. Darawish, B. Burkhardt, T. Dumslaff, X.-Y. Wang, A. Narita, K. Müllen, V. Meunier, R. Fasel, M. Calame, P. Ruffieux, *ArXiv190701797 Cond-Mat* **2019**.